Extreme singular events associated with inertial-viscous cusp formation in fluids

Cite as: Phys. Fluids **32**, 062104 (2020); https://doi.org/10.1063/5.0010421
Submitted: 10 April 2020 . Accepted: 27 May 2020 . Published Online: 12 June 2020

D. Krishna Raja, S. P. Das, and E. J. Hopfinger

Physics of Fluids ARTICLE scitation.org/journal/phf

Extreme singular events associated with inertial-viscous cusp formation in fluids

Cite as: Phys. Fluids 32, 062104 (2020); doi: 10.1063/5.0010421
Submitted: 10 April 2020 • Accepted: 27 May 2020 •
Published Online: 12 June 2020

D. Krishna Raja,[1] S. P. Das,[1,a)] and E. J. Hopfinger[2]

AFFILIATIONS

[1] Department of Mechanical Engineering, Indian Institute of Technology Madras, Chennai 600036, India
[2] LEGI, CNRS/UGA, CS 40700, 38052 Grenoble, France

[a)] **Author to whom correspondence should be addressed:** spdas@iitm.ac.in

ABSTRACT

Cusp singularities in fluids have been experimentally demonstrated in the past only at a low Reynolds number, $Re \ll 1$, and large capillary number, $Ca \gg 1$, in Newtonian or non-Newtonian fluids. Here, we show that the collapse of a free surface wave depression cavity can lead to inertial-viscous cusp formation at local $Re > 1$ and $Ca > 1$, which gives rise to extreme events, i.e., very high-velocity surface jets. The cavities are generated in a cylindrical container ($2R = 10$ cm), partially filled with glycerine–water solution, by parametrically forcing the axi-symmetric wave mode beyond the breaking limit. By varying the forcing amplitude and the fluid viscosity, parabolic or cusp singularities manifest, depending on the last stable wave amplitude b that determines the cavity shape. Cusp formation in collapse without bubble pinch-off, leading to very high-velocity surface jets, is obtained when b is close to the singular wave amplitude b_s and $Ca > 1$. The free surface shape is self-similar, changing from an inertial to a viscous regime when the singularity is approached. At cusp singularity, the cavity shape takes the form of $(z - Z_0)/R \sim -(r/R)^{2/3}$, where Z_0 is the final cavity depth. Cavity collapse with bubble pinch-off, which occurs when $b > b_s$, also exhibits a cusp singularity when $b_s < b \leq 1.14\, b_s$ and $Ca > 1$, but surface jet velocities are much less because about half of the wave energy is lost.

I. INTRODUCTION

Singular events have attracted physicists over decades.[1] Cusp singularities have been identified and applied in the context of gravitational lensing,[2] in optics, leading to bright spots,[3] in biological systems,[4] and in tsunami amplification using ray theory.[5] In two dimensional Stokes flow, Richardson[6] theoretically investigated an inviscid bubble in shear and pure straining flow separately. In both cases, for an extreme condition of zero surface tension, a cusp is formed. In this analysis, the cusp is a two dimensional counterpart of the Taylor[7] experiment of shear and pure straining flow. Experimentally, cusp singularities in fluids have been demonstrated only at a low Reynolds number, $Re \ll 1$, and large capillary number, $Ca \gg 1$, in Newtonian[8] or non-Newtonian fluids.[9,10] Jeong and Moffatt[8] generated cusps by rotating submerged cylinders in a range of low Reynolds numbers (based on angular velocity and cylinder radius), $0 < Re \leq 0.25$, and large capillary numbers, $0 < Ca \leq 61$. At a critical angular velocity, the interface takes the form of a downward pointing cusp represented by $y = c\, x^{2/3}$, where x and y are the cavity width and depth, respectively, and c is a constant of order one. These curvature singularities are line singularities. Point singularities have been described by Taylor,[7,11] Buckmaster,[12] Hinch and Acrivos,[13] and Sherwood.[14]

The free surface cavity and bubble collapse have been associated with conical[15,16] or parabolic shapes.[17–19] The collapse gives rise to high-velocity surface jets and sometimes bubble pinch-off at the cavity base during the collapse, in which case the jet velocity is lower. Zeff *et al.*[17] observed jet velocities as high as 52 m/s using high viscosity glycerine–water solution as the working fluid and scaled the experimentally obtained jet velocities by a capillary velocity. Later, Das and Hopfinger and[18] Raja, Das, and Hopfinger[19] suggested an inertial scaling in good agreement with experiments. By contrast, surface bubble collapse is driven by capillary forces,[20–24] in which case Ca is always $Ca \ll 1$.

In this paper, we demonstrate, for the first time, that the relatively large Reynolds number inertial cavity collapse can lead to extreme events, i.e., emerging jet velocities of 120 m/s or larger, associated with cusp singularities. These extreme singular events

manifest when at singular collapse, the local capillary number $Ca > 1$ and the last stable wave amplitude b that determines the cavity shape are close to the singular wave amplitude b_s. When $b > b_s$, bubble pinch-off occurs, and jet velocities are much less even though cusp formation is observed when $b_s \leq 1.14$ and $Ca > 1$.

The experimental conditions and procedures are presented in Sec. II. Then, in Sec. III, the results of no pinch-off cavity collapse are discussed, by first presenting the self-similarity in the inertial and viscous regimes and then the conditions of cusp formation, followed by the theoretical formulation of cusp geometries. In Sec. IV, cavity collapse with pinch-off and possible cusp formation is discussed. Jet velocities are analyzed in Sec. V, followed by conclusions in Sec. VI.

II. EXPERIMENTAL CONDITIONS

The experiments have been conducted in a circular cylindrical container, made of plexiglas, of diameter $2R = 10$ cm and 10 cm deep, mounted on a vertically oscillating vibration exciter (Model: APS 400 ELECTRO-SEIS) of peak force 440 N. After calibration, the vibration amplitude was kept within ±0.30% of the nominal value and the frequency within 0.02%. The container was partially filled with glycerine–water (GW) solutions of kinematic viscosities $\nu = 0.09$ cm^2/s (GW 60) and 0.5 cm^2/s (GW 80). Here, 60 and 80 stand for the percentage by volume of glycerine in the solution. The surface tension is $\sigma \cong 0.067$ N/m and the density is $\rho = 1160$ kg/m^3 for GW 60 and 0.064 N/m and 1205 kg/m^3 for GW 80, respectively. As in previous experiments,[17,19] the wave motions were parametrically excited by accelerating the container at ω_f, twice the axi-symmetric mode wave frequency ω, in the form $a(t) = A \sin \omega_f t$, where A is the amplitude of container motion. The stability boundaries for the two viscosity fluids used are, respectively, $(A/R)_c = 0.006$ and 0.013 with associated frequencies $\omega_0 = 28.20$ rad/s and 28.10 rad/s. Large amplitude standing waves are obtained by overdriving the system at $A/R > (A/R)_b$ and slightly off resonance, i.e., $\omega_f/2\omega_0 = 0.995$, where $(A/R)_b$ is the wave breaking threshold. In the Appendix, the instability threshold $(A/R)_c$ and wave breaking boundaries $(A/R)_b$ for both GW 60 and GW 80 are shown. The Reynolds and Weber numbers are $Re = \omega_0 R^2/\nu = 7833$ and 1405 and $We = \rho\omega_0{}^2 R^3/\sigma = 1709$ and 1858, respectively, giving global capillary numbers $Ca = \omega_0 R\mu/\sigma = 0.22$ and 1.32. The experiments have been started each time from an unperturbed condition, i.e., interface at rest. The last stable wave amplitude depends on the rate of increase in forcing amplitude (on A/R). Fine-tuning is required to obtain the wave amplitude b_s ($b_s/R = 1.002$), called the singular wave amplitude, at which the jet velocity is highest. The displacement of the shaker has been measured using a Wenglor CP24 laser displacement sensor with a resolution of 20 μm.

Wave amplitude and wave trough shapes are measured by visualizations and image analysis only. A Photron FASTCAM Mini UX100 high-speed camera is used to capture the interface with an acquisition speed of 2000–10 000 fps. Concerning the measurement of jet velocity, Raja, Das, and Hopfinger[19] showed that the vertical retraction speed of the singular cavity depth $Z_0(t_0)$ is equal to the jet velocities. Thus, jet velocities have been determined from the distance moved by the jet in the time interval $(t_s - t_0)$, from Z_0 at time t_0 to the position above the free surface where the jet has been seen first at time t_s.

III. NO PINCH-OFF CAVITY COLLAPSE

A. Self-similarity of collapse

No pinch-off cavity collapse is obtained when the last stable wave amplitude $b \leq b_s$ ($b_s/R = 1.002$ in the present experiments). The different stages of no pinch-off cavity collapse are presented in Fig. 1. Figure 1(a) shows a composite image of the last wave amplitude b and the wave depression cavity of radius r_i. The cavity radius $r(z, t)$ at any instant of time τ during the collapse is shown in Fig. 1(b), and the final cavity shape (lower half) and jet appearance (upper half) are shown in Fig. 1(c). Here, the minimum radius is $r_m = r(Z, t)$, and Z_0 is the final cavity depth measured from the free surface at $\tau = 0$ where $\tau = (t_0 - t)$, with t_0 being the time at singularity.

The change in minimum cavity radius $r_m = r(Z, t)$ as a function of τ in GW 80 for wave amplitude $b \simeq b_s$ is shown in Fig. 2. Two self-similar regimes are clearly identified, with the first regime being inertial with a time dependency of cavity radius r_m varying as $r_m \propto \tau^{1/2}$, followed by a viscous regime with time dependency

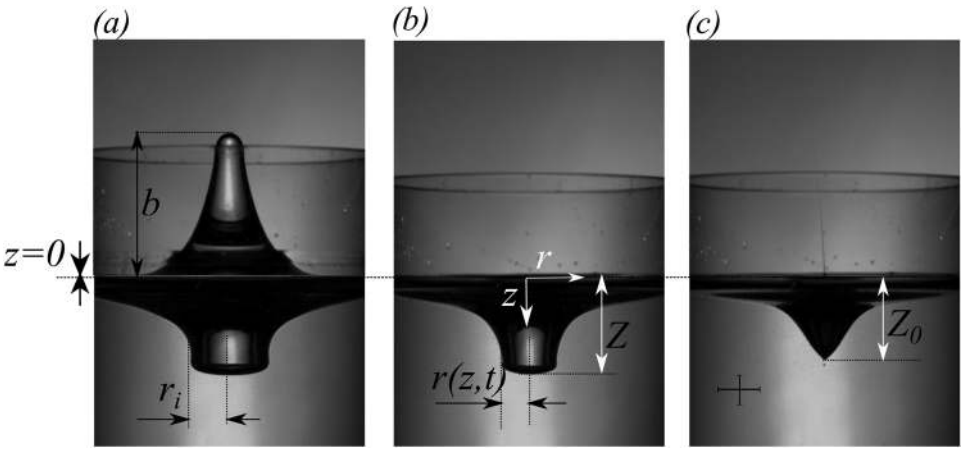

FIG. 1. Cavity shapes without pinch-off and definitions of b, Z_0, $Z(t)$, r_i, and $r(z, t)$. Composite image of (a) the last wave amplitude b (upper half) and initial cavity shape (lower half), (b) cavity shape at an intermediate time, and (c) final cavity shape (lower half) at $t = t_0$ and jet formation (upper half). The dotted horizontal line corresponds to $z = 0$. The scale bars represent 1 cm.

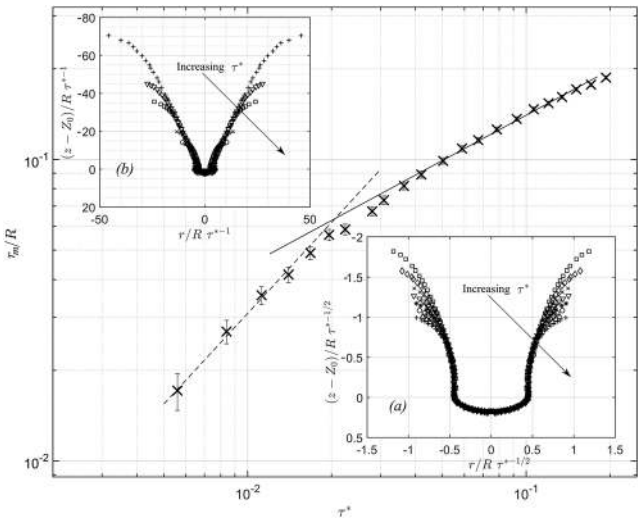

FIG. 2. Change in minimum cavity radius [$r_m = r(z = Z, t)$] as a function of $\tau^* = \tau/\sqrt{R/g}$ in GW 80 ($\nu = 0.5$ cm^2/s), where $\tau = (t_0 - t)$ is the time remaining to singularity. The forcing amplitude is $A/R = 0.0340$, giving $b \simeq b_s$. In the initial stage of cavity collapse, the change in the cavity radius follows $r_m/R \propto \tau^{*1/2}$ with a gradual crossover in the late stage of collapse to $r_m/R \propto \tau^*$. The solid and dashed lines show slopes 0.5 and 1, respectively. Inset (a): cavity shapes in the inertial regime at eight different instants 10 ms, 9 ms, 8 ms, 7 ms, 6 ms, 5 ms, 4 ms, and 3 ms before singularity, showing a self-similar behavior when scaled with $\tau^{*1/2}$ and the container radius R. Inset (b): cavity shapes in the viscous regime at 2 ms, 1.4 ms, 0.8 ms, 0.6 ms, 0.4 ms, and 0.2 ms before singularity, showing self-similarity when scaled with τ and the container radius R. Z_0 is the final cavity depth (corresponding to $\tau = 0$), measured from the free surface ($z = 0$).

$r_m \propto \tau$. Similar power-law behaviors have been identified in the collapse of the crater/cavity generated by disk impact on a free surface,[25,26] drop impact on liquid pool,[27] and wave depression cavities.[19] The collapse of a small hole in fluid sheet[28] also indicates a similar behavior with an early inertial regime and late Stokes regime close to collapse.

B. Singular collapse and cusp formation

The cavities considered in the present experiments are inertia driven, similar to the impact generated cavities. In the viscous regime, for conditions corresponding to Fig. 2 ($Ca > 1$ and $b/b_s \simeq 1$), a cusp forms at the cavity base, which has geometric similarities with cusps in Stokes flow, investigated by Jeong and Moffatt,[8] in the highly viscous liquid ($\nu = 0.014$ m^2/s) at $Re \ll 1$ and $Ca \gg 1$, based on the rotation speed of submerged counter-rotating cylinders that drive the flow. These cusps are of generic form $y = c\,x^{2/3}$, earlier shown by Joseph *et al.*[9] for non-Newtonian viscous fluids. Joseph *et al.*[9] also demonstrated cusp formation with rotating cylinders in liquids of low surface tension where the cusp geometry is also of the form $y = c\,x^{2/3}$, with the value of c determined close to the cusping point.

In the present experiments with GW 80, the Reynolds number based on the cavity radius r_m and radial velocity, $U_r = \delta r_m/\delta t$, is in the inertial range (Fig. 2, inset a), $Re_I = (U_r r_m/\nu)_I \approx 66$ and the Weber number $We_I = (\rho U_r{}^2 r_m/\sigma)_I \approx 22.4$. In the viscous range (Fig. 2, inset b), $Re_v \approx 43$ and $We_v \approx 103$, giving a local capillary number $Ca = We_v/Re_v \approx 2.4$, indicating that viscous forces are dominating over capillarity. We observe that in this case, when the system is driven at $A/R = 0.0340$ such that $b \simeq b_s$, the extreme singular event leads to jet formation, with the jet velocity $U_j \approx 120 \pm 20$ m/s. The corresponding singularity shape is a cusp [Fig. 3(b)]. At lower viscosity, (here in GW 60 of $\nu = 0.09$ cm^2/s, giving a capillary number $Ca = 0.40$), capillary forces dominate the late stage of singular collapse preventing cusp formation, as shown in Fig. 3(a). Experiments conducted with a glycerine–water solution ($\nu = 2.16$ cm^2/s) also exhibit a cusp singularity at collapse, but the maximum jet velocity here drops to 80 m/s because of viscous damping. The experiments by Zeff *et al.*[17] conducted in fluids of similar viscosity showed, surprisingly, a parabolic cavity shape.

In surface bubble collapse, cusp formation is not possible because the collapse is driven by capillary forces with the length scales varying as $\tau^{2/3}$.[24] Hence, in the capillary number $Ca = \mu U/\sigma$, the velocity U scales with the capillary velocity, $U = \alpha\, U_c = \alpha\sqrt{\sigma/\rho R_0}$, where R_0 is the bubble radius, giving $Ca = \alpha\mu/(\rho\sigma R_0^2)^{1/2} = \alpha\, Oh$. When $Oh \ll 1$[22,23] and $\alpha = \mathcal{O}(10)$, we get $Ca < 1$, which means that cusp formation is not possible. However, when gravity effects are negligible, i.e., $Bo = \rho g R_0^2/\sigma < 0.1$, viscosity is necessary for the reversal of the curvature at the bubble base, and jet initiation depends on the Ohnesorge number.[22,23] More recently, Gordillo and Rodríguez-Rodríguez[29] found that the jet velocity increases with the Oh number for bubble collapse with $Bo = 0.05$, reaching a maximum at $Oh = Oh_c$, which corresponds to the conical shape of the bubble cavity at collapse.

C. Theoretical description of cusp geometries

Geometrically, a cusp is formed by the trajectory of a point attached to the perimeter of a disk rolling on a flat surface. A loop or parabola is generated when the point is displaced from the perimeter by a small parameter ε. The generic form of the curve close to singularity[30] is

$$x = \varepsilon\eta + \frac{\beta}{3}\eta^3 \quad \text{and} \quad y = \frac{\eta^2}{2}. \tag{1}$$

Adding a translation in y, Eq. (1) can be written as

$$x^2 = 2\varepsilon^2(y+\zeta) + \frac{8\beta^2(y+\zeta)^3}{9} + \frac{8\beta\varepsilon(y+\zeta)^2}{3} \tag{2}$$

such that $\varepsilon = 0$ gives a cusp of the form $(y + \zeta) = (1/2)(3/\beta)^{2/3}x^{2/3}$. Here, β is a constant, which determines the strength of the cusp.

In viscous fluids, Jeong and Moffatt[8] used conformal mapping to express the free surface by

$$x = a\,\cos\theta + \frac{(a+1)\cos\theta}{1+\sin\theta} \quad \text{and} \quad y = a\,(1+\sin\theta). \tag{3}$$

Singularity conditions require that $dx/d\theta = dy/d\theta = 0$ at the singular point, which is satisfied when $\theta = \pi/2$ and $a = -1/3$. Expanding Eq. (3) in the neighborhood of the singular point, using $a = -1/3 + \varepsilon$ and $\theta = \pi/2 + \eta$, leads to the parametric form $x = -(3/2)\varepsilon\eta - \eta^3/12$ and $y = -2/3 + 2\varepsilon + \eta^2/6$, which is equivalent to Eq. (1), hence also Eq. (2), when applying a translation such that $y = \eta^2/6$. Different values of the small parameter ε represent the shape of the

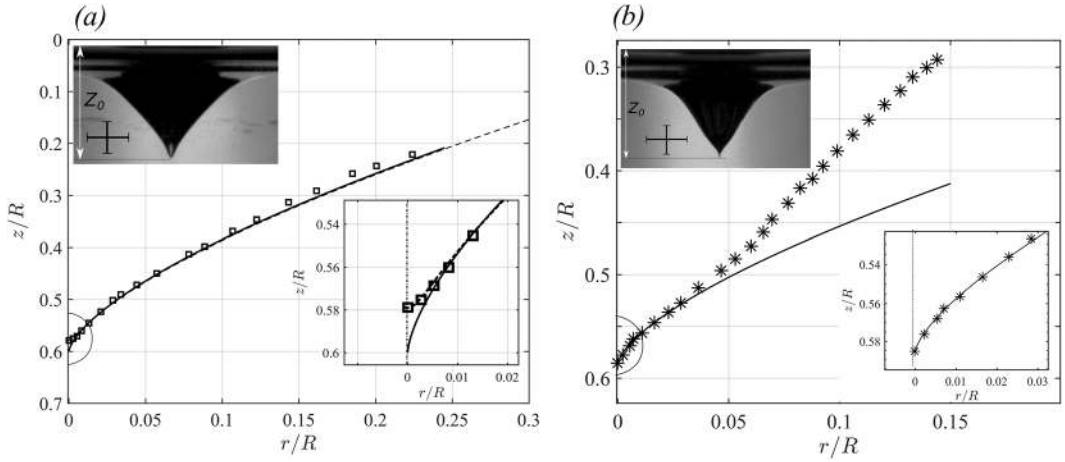

FIG. 3. Final cavity surface when $b/b_s \simeq 1$ in (a) GW 60 and (b) GW 80. In (a), the experimental points □ are fitted by $(z - Z)/R = -c\,(r/R)^{2/3}$ (solid line), with $c = 1$ (here $Z/R = 0.6$). The dashed curve is given by Eq. (2) with $\varepsilon = 0.05$, which is close to $\varepsilon \approx \exp(-2\pi Ca) \approx 0.08$, $\zeta = 0.579$, and $\beta = 1.06$. The inset on the right in (a) shows an enlarged view of the cavity tip indicating a parabolic shape. (b) Final cavity surface in GW 80, experimental points ∗, compared with Eq. (2), which, in the $(r/R, z/R)$ plane for $\varepsilon = 0$ [$\varepsilon \approx \exp(-2\pi Ca) \sim 10^{-7}$], $\zeta = 0.586$, and $\beta = 2.2$, reduces to $z/R - 0.586 = -0.615(r/R)^{2/3}$. The enlarged view of the cavity tip (inset on the lower right) shows a cusp. The insets at the left-hand side in (a) and (b) show images of the cavity tip shapes. The horizontal and vertical bars represent 1 cm.

curve in the neighborhood of the singular point, as shown in Fig. 4. A cusp singularity is obtained for $\varepsilon = 0$. At singularity, Fig. 4(a) can also be represented by Eq. (2) with $\beta = 1/\sqrt{3}$ and $\zeta = 2/3 - 2\varepsilon$. The cavity profiles of the present experiments can be fitted by Eq. (2) by adjusting the parameters ζ and β. The free surface shapes of Jeong and Moffatt[8] leading to a cusp are two dimensional curvatures. In the present case, for axi-symmetric collapse, $y \equiv -z/R$, $x \equiv r/R$, and $\zeta \equiv Z/R$ so that taking in Eq. (2), $\beta = 1.06$ and $\varepsilon = 0$, the final free surface cavity boundary takes the form $(z - Z)/R = -(r/R)^{2/3}$. In Fig. 3(a), the measured final cavity surface shape in GW 60 is compared with the form $(z - Z)/R = -(r/R)^{2/3}$ [solid line in Fig. 3(a)] with $Z/R = 0.6$. In the enlarged view of the tip [inset in Fig. 3(a)], the measured shape shows a stagnation point (parabolic shape) as in Fig. 5 in the work of Jeong and Moffatt.[8] With $\varepsilon = 0.05$ in Eq. (2), good agreement is obtained with a parabolic tip, as shown by the dashed line in the inset of Fig. 3(a). In Fig. 3(b), the measured final free surface in GW 80 is compared with a cusp form represented by Eq. (2), with $\varepsilon = 0$ and $\beta = 2.2$. There exists a genuine cusp singularity, highlighted in the inset of Fig. 3(b), in good agreement with the cusp geometry of Eq. (2). Figures 5(a) and 5(b) show, in the doubly logarithmic plot, the final cavity shape in GW 60 and GW 80, respectively; there is excellent agreement with Eq. (2) with $\varepsilon = 0.05$ in GW 60 and $\varepsilon = 0$ in GW 80. This demonstrates that because of the exponential dependency of the cavity base radius on the capillary number,[8] relatively small changes in the capillary number have a large effect on the cavity base radius. According to Eggers and Fontelos,[30] citing Hinch, ε varies as $\varepsilon \approx \exp(-2\pi Ca)$. For GW 60, we get $\varepsilon \approx 0.08$; the cavity base is parabolic [Fig. 3(a)]. For $Ca = 2.4$ and $\varepsilon \approx 10^{-7} \to 0$, a cusp is formed [Fig. 3(b)].

The foregoing results have been obtained when $b \simeq b_s$. When the last wave amplitude is less, $b \approx 0.93\, b_s$, the cavity tip is parabolic, as shown in Fig. 6, even though $Ca > 1$. In Figs. 6(a) and 6(b), the initial and final cavity shapes generated, respectively, by the last wave amplitudes $b \simeq b_s$ and $b \simeq 0.93\, b_s$ are compared; the final cavity shape when $b/b_s \simeq 0.93$ is in good agreement with Eq. (2) with $\varepsilon \approx 0.05$ and $\beta = 1.8$, indicating a parabolic shape. Thus, for cusp formation, a certain initial cavity shape, which depends on the last wave amplitude, is required in addition to $Ca > 1$.

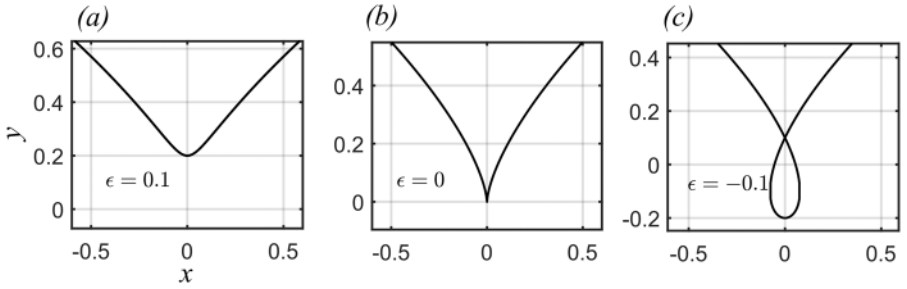

FIG. 4. Curves representing the parametric form $x = -(3\varepsilon/2)\eta - \eta^3/12$ and $y = 2\varepsilon + \eta^2/6$ (translating y to the origin), obtained from Eq. (3) using $a = -1/3 + \varepsilon$ and $\theta = \pi/2 + \eta$ in the neighborhood of singularity. (a) $\varepsilon = 0.1$, (b) $\varepsilon = 0$, giving a cusp shape $y = 0.874\, x^{2/3}$, and (c) loop for $\varepsilon = -0.1$.

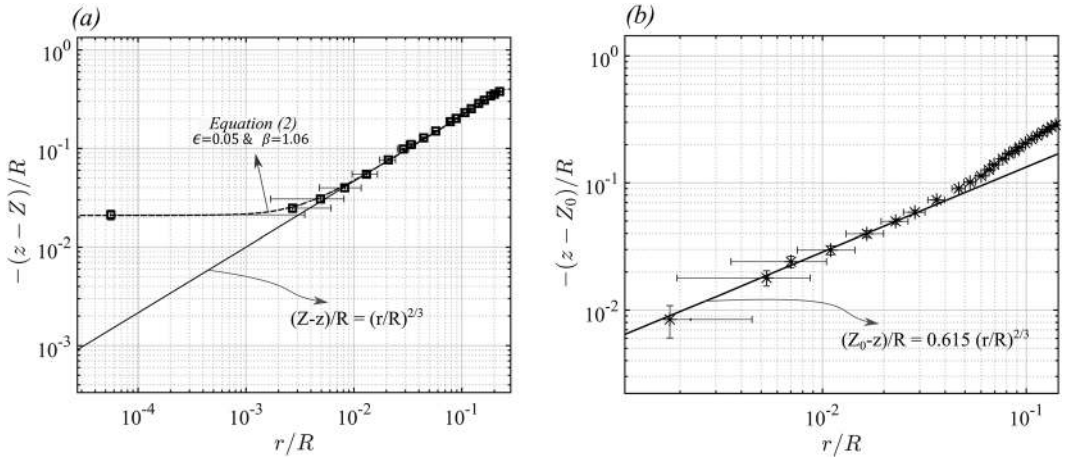

FIG. 5. Log–log plot of final cavity shapes with origins shifted to the cusp tip: (a) GW 60 (□), where the solid and dashed lines represent $(Z - z)/R = (r/R)^{2/3}$ and Eq. (2) with $\varepsilon = 0.05$ and $\beta = 1.06$, respectively, and (b) final cavity shape in GW 80 (∗), compared with Eq. (2). Conditions are the same as in Fig. 3.

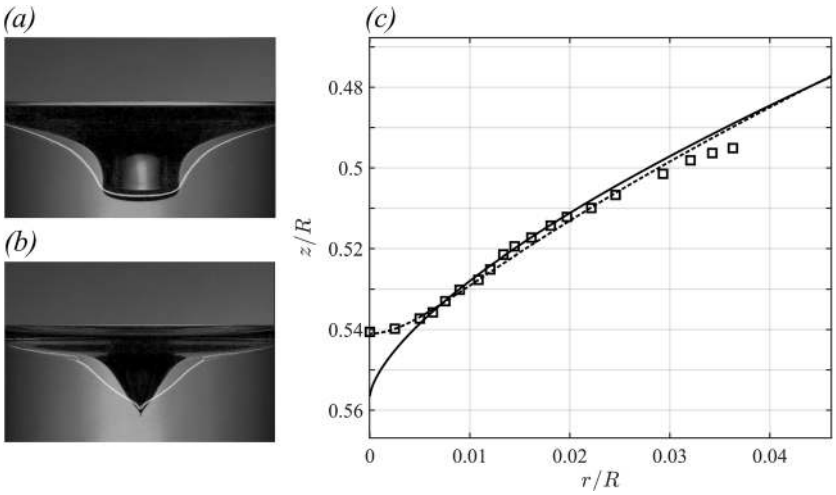

FIG. 6. Comparison of (a) the initial cavity shapes in GW 80 for $b \simeq b_s$ (grayscale images) and $b/b_s \simeq 0.93$ (white line) and (b) singular cavity shapes. (c) Experimental final cavity shape for $b/b_s \simeq 0.93$ compared with Eq. (2) using $\varepsilon \approx 0.05$ and $\beta = 1.8$, indicated by a dashed line. For comparison, a cusp $(z/R - 0.5565) = -0.615\,(r/R)^{2/3}$ is shown by the solid line.

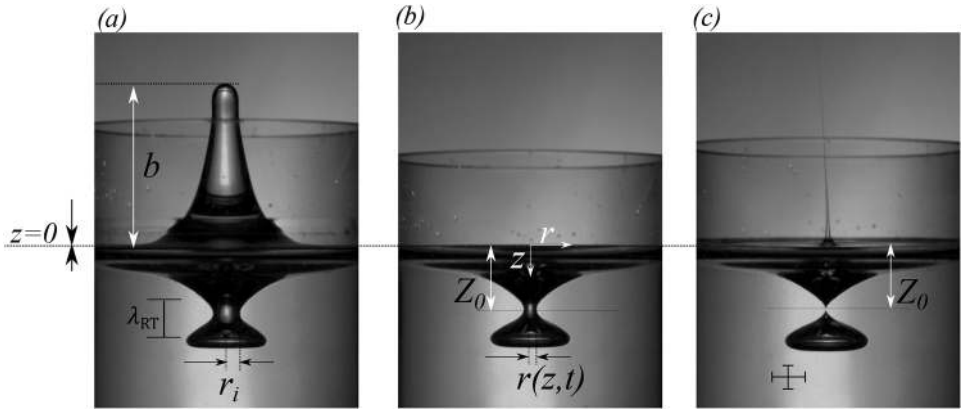

FIG. 7. Cavity shapes with pinch-off and definitions of b, Z_0, r_i, and $r(z, t)$. (a) Composite image of last wave amplitude $b > b_s$ and the full-grown cavity depth of radius r_i, (b) cavity shape at an intermediate time during collapse, and (c) composite image of bubble pinch-off at the cavity base and jet formation above.

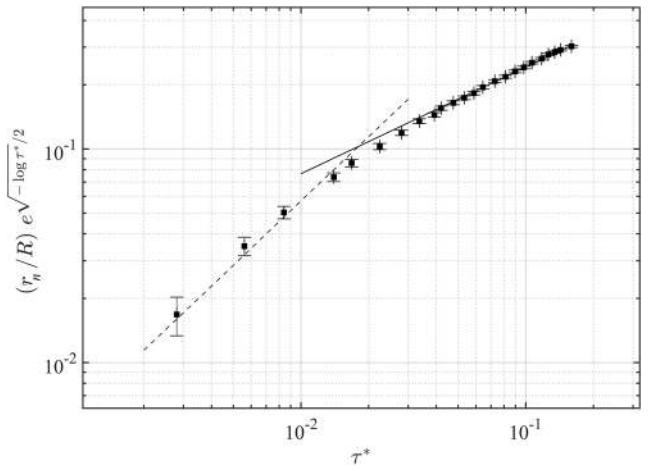

FIG. 8. Logarithmic corrected[31] neck radius $(r_n/R)\ \exp\left(\sqrt{-\log \tau^*}/2\right)$ in GW 80 as a function of time $\tau^* = \tau/\sqrt{R/g}$. The forcing amplitude is $A/R = 0.0365$ and $b/b_s = 1.14$. ■ indicates experiments; the solid line indicates a slope of $\frac{1}{2}$, and the dashed line shows a slope of 1.

IV. CAVITY COLLAPSE WITH PINCH-OFF

Pinch-off occurs when the last stable wave amplitude $b > b_s$. The definitions of b, r_i, $r(z, t)$, and Z_0 are shown in Fig. 7. The neck radius at any instant of time is here $r_n = r(z = Z_0, t)$ [Figs. 7(b)], and Z_0 is the effective cavity depth, which is the pinch-off location [Fig. 7(c)]. The velocity field at the pinch-off location is radially inward.[26] A plausible reason for pinch-off is that there is onset of Rayleigh–Taylor instability at the lower cavity boundary during the downward wave deceleration $a \approx 3g$. The most unstable wavelength is then $\lambda_{RT} = 2\pi\sqrt{3\sigma/\rho a} \approx 1.4$ cm, which is indicated in Fig. 7(a).

When $b > b_s$, the cylindrical portion of the wave cavity, as shown in Fig. 1(a), exceeds the critical wavelength λ_{RT}, which initiates cavity pinch-off. The variation of the neck radius with time in pinch-off cavity collapse exhibits a power-law similar to no pinch-off collapse (Fig. 2), but with a larger time exponent (>1/2) in the inertial regime. The collapse dynamics is similar to disk impact[25] on fluid or pinch-off of a bubble issuing from a submerged nozzle.[32,33] Gas bubble pinch-off exhibits power-law behavior with the exponent varying with fluid viscosity such that the neck radius is proportional to $\tau^{1/2}$ for less viscous fluids and to τ in highly viscous fluids.[34,35] In their experiments with Newtonian fluids, Jiang, Zhu, and Li[35] observed a cusp shape for high viscous fluids and "tail" for non-Newtonian fluids. In coalescence of circular lenses in water, a viscous-inertial crossover has been identified with a smooth transition from $r \propto \tau$ to $r \propto \tau^{1/2}$, where τ is here the time after initial contact.[36] Considering the crossover between viscous-inertial regimes, Xia, He, and Zhang[37] developed a master curve capturing the full range of coalescence dynamics for different fluid viscosities. Axisymmetric bubble pinch-off[38] or cavity pinch-off[25] is logarithmically slow, i.e., the time exponent relies on logarithmic terms such that $r(-\log r)^{1/4} \propto \tau^{1/2}$[39] and $r \propto \tau^{1/2} e^{-\sqrt{-\log \tau}/2}$.[31] Fontelos, Snoeijer, and Eggers[40] developed a theory of the spatial structure of bubble pinch-off in the low viscosity fluid. This confirms that collapse is logarithmically slow and can be expressed in terms of the square of the aspect ratio of the neck radius to the axial extent of pinch-off, in good agreement with experiments.[25,32] Figure 8 shows the time evolution of the neck radius, $(r_n/R)\ \exp\left(\sqrt{-\log \tau^*}/2\right) \propto \tau^{*1/2}$. At the late stage, the neck radius r_n is linear in τ^*, which indicates a viscous transition. In the case of no pinch-off cavity collapse (Fig. 2), a logarithmic term was not necessary because the cavity collapses radially and axially. Figure 9 shows the final surface shape at pinch-off. Cusp formation at the pinch-off position is identified, as shown in the semi-logarithmic plot [Fig. 9(b)], where experiments are compared with $(z - Z_0)/R = \pm c\ (r/R)^{2/3}$. Best fit with the experimental data is obtained with

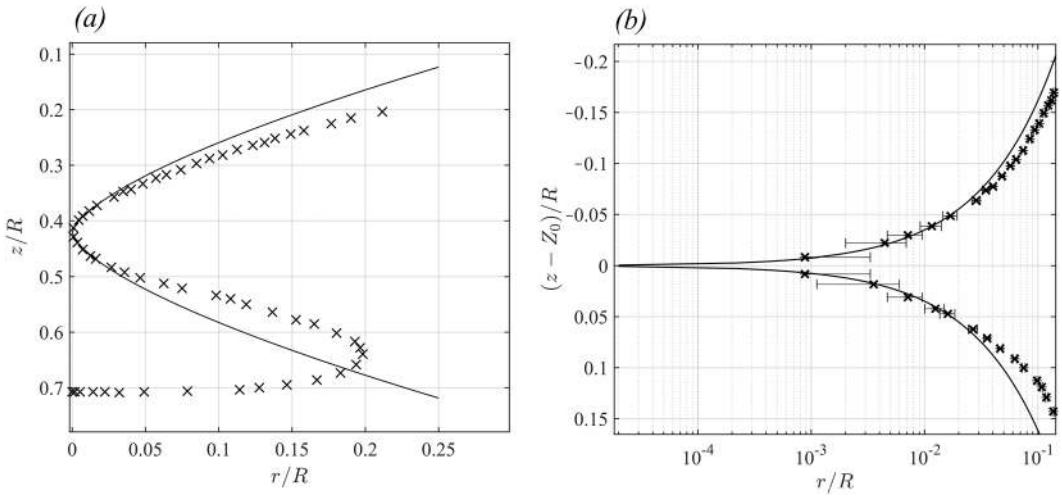

FIG. 9. Final surface shape at pinch-off in GW 80 ($A/R = 0.0365, b/b_s = 1.14$). The solid line curves are given by Eq. (2) with $\epsilon \approx 0$, $\beta = 1.64$, and $\zeta = 0.42$ such that $z/R - 0.42 = \pm 0.75(r/R)^{2/3}$. (a) ×, represents the cavity shape at $t - t_0$. (b) Semi-log plot of the final cavity shape with the origin shifted to pinch-off location Z_0.

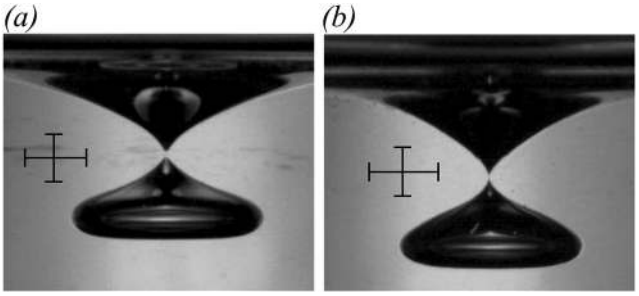

FIG. 10. Cavity shapes at pinch-off. (a) GW 60, b/b_s = 1.08 and (b) GW 80, b/b_s = 1.14. The scale bars represent 1 cm.

$c = 0.75$. Away from the singular location, and especially below it, i.e., $z > Z_0$, the free surface boundary notably deviates from the theoretical surface topology because the cavity is not open but surrounded by liquid underneath the air. It is important to note that cusp formation at the pinch-off location occurs in GW 80 [Fig. 10(b)], where the local capillary number $Ca > 1$ in addition to $b \leq 1.14\ b_s$. In GW 60, capillary forces dominate ($Ca < 1$), and the shape is parabolic after pinch-off [Fig. 10(a)].

V. JET VELOCITIES

Dimensionless jet velocities $U_j/\sqrt{gR}$ in glycerine water GW 80 ($\nu = 0.5$ cm^2/s), measured as in the work of Raja, Das, and Hopfinger[19] (see Sec. II), are shown in Fig. 11 as a function of b/b_s. The experimental points compare well with the singular scaling $U_j/\sqrt{gR} = C_1(b/R)[b/(|b - b_s|)]^{1/2}$[19] corresponding to the solid lines obtained with the prefactor $C_1 = 14$. The singular amplitude is $b_s/R = 1.002$, where the velocity can theoretically be infinite with the jet diameter going to zero. However, viscosity prevents this to happen. Composite images of cavity shape at time t_0 below and jets above are shown in the insets of Fig. 11. The novelty here is the cusp formation at the cavity base when $b \simeq b_s$ (see inset b), as demonstrated in Fig. 3(b), giving rise to very high-velocity surface jets, here, of velocity 120 ± 20 m/s or higher. The jet energy is $E_j \approx \frac{\pi}{2}\rho {U_j}^2 {r_j}^2 Z_0$, and wave energy is evaluated as $E_w \approx \frac{1}{25}\pi\rho g b^2 R^2$, giving a ratio $\frac{E_j}{E_w} \lesssim 0.70$, for $U_j = 120$ m/s with $b \approx R$, $Z_0 \approx 0.6R$, and $r_j \lesssim R/550$. As the last stable wave amplitude approaches the critical value b_s, the singular scaling[17,19] predicts that the velocity diverges and further increase in forcing amplitude such that $b > b_s$ leads to cavity collapse with bubble pinch-off (inset c). In this case, at the pinch-off position, the cavity has also a cusp shape, but the jet velocity is $U_j \lesssim 33 \pm 1.6$ m/s only. The decrease in jet velocity is mainly because of loss of wave energy due to bubble pinch-off. This loss is $\Delta E_w = E_w\left(1 - \frac{E_{wP}}{E_w}\right)$, where wave energy after pinch-off is given as $E_{wP} \approx \frac{1}{25}\pi\rho g {b_P}^2 R^2$, with effective wave amplitude $b_P \approx 1.7\ (Z_0)_P$. Thus, the loss is $\Delta E_w \approx E_w\left(1 - \frac{(Z_0^2)_P}{Z_0^2}\right) \approx 0.5E_w$. When b is further increased, the cavity tip is parabolic just after pinch-off (inset d). Thus, cusp singularities exist when $0.97 \lesssim b/b_s \lesssim 1.14$, but these lead to high jet velocities only when $b/b_s \lesssim 1$. For wave amplitudes $b/b_s < 0.97$ or $b/b_s > 1.14$, the cavity shapes (at t_0) are no longer cusp-like, and jet velocities decrease rapidly. The capillary and Reynolds numbers have values similar to those of $b/b_s < 0.97$ and $b/b_s > 1.14$. However, the cavity aspect ratio of width to depth increases [see Figs. 6(b), 11(a), and 11(d)] with an increase in deviation of b from b_s.

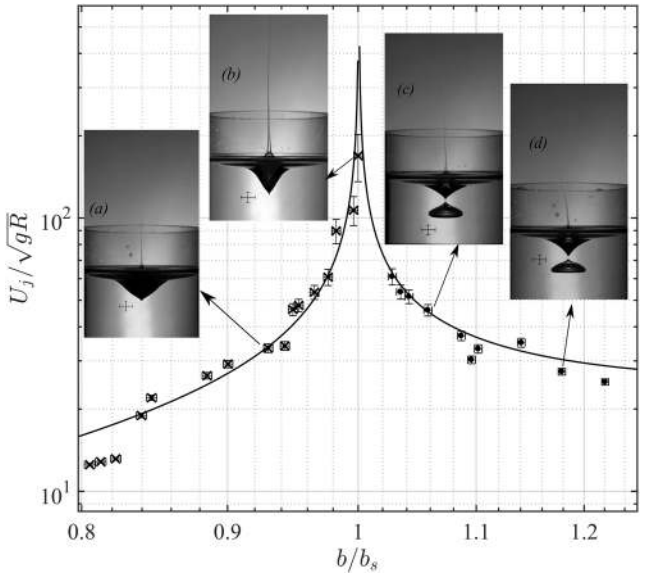

FIG. 11. Log–log plot of dimensionless jet velocity $U_j/\sqrt{gR}$ as a function of last wave amplitude b/b_s, where $b_s/R = 1.002$. The symbols × and • show the measured jet velocities for no pinch-off and pinch-off cavity collapse, respectively. The solid line shows the theoretical curve given by the singular scaling $U_j/\sqrt{gR} = C_1(b/R)[b/(|b - b_s|)]^{1/2}$. Insets a and b show the composite images of wave depression cavity collapse and jet formation for no-pinch, $b \leq b_s$, and insets c and d for pinch-off, $b > b_s$. When $b \simeq b_s$ ($A/R = 0.0340$, inset b), the jet velocity just above the undisturbed free surface is $U_j = 120 \pm 20$ m/s. In the case of bubble pinch-off, $b > b_s$ for $A/R = 0.0358$ (inset c), $U_j = 33 \pm 1.6$ m/s even though the cavity tip after pinch-off is a cusp. Further away from the singular amplitude at $b/b_s < 0.97$ (inset a) and $b/b_s > 1.14$ (inset d), jet velocities are much less, and the cavity tips are parabolic (inset d). The images of the jets have been taken at 10 ms after emergence from the free surface. The horizontal and vertical bars represent 1 cm.

VI. CONCLUSIONS

The present experiments demonstrate that collapse ($Re \gg 1$) of a free surface wave depression cavity leads to inertial-viscous cusp formation when (i) the local capillary number at collapse is $Ca > 1$ and (ii) the cavity depth to radius ratio is appropriate, which can be monitored through the last stable wave amplitude b with respect to the singular wave amplitude b_s. The singular wave amplitude determines the change from no pinch-off ($b < b_s$) to pinch-off ($b > b_s$). Cusp formation in no pinch-off collapse gives rise to extreme events, i.e., very high-velocity surface jets, here $U_j \approx 120 \pm 20$ m/s when $b \simeq b_s$. The free surface shape is self-similar, changing from an inertial to a viscous regime when the singularity is approached. At cusp singularity, the cavity shape takes the form of $(z - Z_0)/R \sim -(r/R)^{2/3}$, where Z_0 is the final cavity depth. When $Ca < 1$, capillary forces prevent cusp formation, and the cavity tip becomes parabolic in shape,

resulting in considerably lower jet velocities. The parabolic cavity shape at collapse also occurs when the last stable wave amplitude $b/b_s < 0.97$ even though $Ca > 1$. For much larger fluid viscosity such that $Ca \gg 1$ with cusp formation, viscosity has a damping effect, and jet ejection speeds are less. Viscosity has a similar damping effect for jetting from bubble bursting, where beyond a critical Oh, i.e., at $Oh > Oh_c(Bo)$, the jet velocity decreases.

Cavity collapse with bubble pinch-off also exhibits cusp formation of shape $z/R - 0.42 = \pm 0.75\ (r/R)^{2/3}$ when $Ca > 1$ and $1 < b/b_s \leq 1.14$. However, jet velocities are much less because more than half of the wave energy is lost by the bubble pinch-off and is thus not available for jet formation. The time evolution of the neck radius is $(r_n/R)\ \exp\left(\sqrt{-\log \tau^*}/2\right) \propto \tau^{*1/2}$ with a viscous transition to $r_n/R \sim \tau^*$ at the late stage of cavity collapse.

It is remarkable that in fluids, parabolic and cusp singularities, as indicated in Fig. 4, can be demonstrated (Figs. 3 and 9).

APPENDIX: INSTABILITY THRESHOLD AND WAVE BREAKING BOUNDARIES

Figure 12 shows the boundaries of instability $(A/R)_c$ and wave breaking thresholds $(A/R)_b$ as a function of forcing frequency. $(A/R)_c$ is the minimum forcing amplitude for the onset of wave appearance at the free surface, and $(A/R)_b$ is the wave breaking threshold amplitude. The solid lines correspond to the weakly nonlinear theory,[41] with the damping estimated from decay experiments. The dashed line indicates $\omega/\omega_0 = 0.995$, at which the experiments have been conducted. For excitation amplitude, $A/R \geq (A/R)_b$, the surface wave grows exponentially and reaches a wave amplitude $b/R \geq 0.8$, which eventually leads to cavity collapse and jet formation. The breaking boundaries for GW 60 and GW 80 are indicated in Fig. 12 by □ and ●.

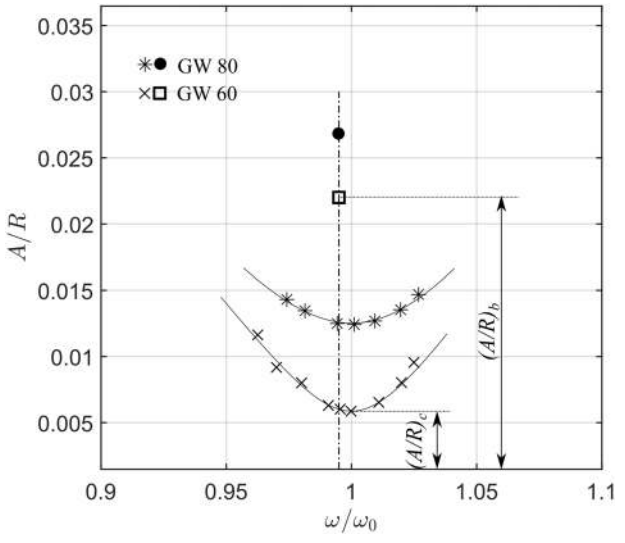

FIG. 12. Dimensionless forcing amplitude (A/R) as a function of frequency, ω/ω_0. The solid lines are the theoretical instability curves.[41] $(A/R)_c$ and $(A/R)_b$ are, respectively, the instability and wave breaking bounds. Symbols × and ∗ show the instability boundaries for GW 60 and GW 80, respectively. □ and ● represent the respective wave breaking threshold. The vertical dashed line refers to conditions at which the jetting experiments are conducted.

ACKNOWLEDGMENTS

We thank Professor Shaikh Faruque Ali, Department of Applied Mechanics and Professor Sabita Sarkar, Department of Metallurgical and Materials Engineering, Indian Institute of Technology Madras for sparing laboratory facilities and equipment to conduct the experiments.

DATA AVAILABILITY

The data that support the findings of this study are available from the corresponding author upon reasonable request.

REFERENCES

[1] T. Poston and I. Stewart, *Catastrophe Theory and its Applications* (Pitman, London, UK, 1996), Reprinted by Dover.
[2] A. O. Petters, H. Levine, and J. Wambsganss, *Singularity Theory and Gravitational Lensing* (Springer Science & Business Media, 2012).
[3] V. I. Arnold, *Catastrophe Theory* (Springer Science & Business Media, 2003).
[4] E. C. Zeeman, "Catastrophe theory," Sci. Am. **234**, 65–83 (1976).
[5] M. V. Berry, "Focused tsunami waves," Proc. R. Soc. A **463**, 3055–3071 (2007).
[6] S. Richardson, "Two-dimensional bubbles in slow viscous flows," J. Fluid Mech. **33**, 475–493 (1968).
[7] G. I. Taylor, "The formation of emulsions in definable fields of flow," Proc. R. Soc. London, Ser. A **146**, 501–523 (1934).
[8] J.-T. Jeong and H. K. Moffatt, "Free-surface cusps associated with flow at low Reynolds number," J. Fluid Mech. **241**, 1–22 (1992).
[9] D. D. Joseph, J. Nelson, M. Renardy, and Y. Renardy, "Two-dimensional cusped interfaces," J. Fluid Mech. **223**, 383–409 (1991).
[10] S. Karpitschka, J. Eggers, A. Pandey, and J. H. Snoeijer, "Cusp-shaped elastic creases and furrows," Phys. Rev. Lett. **119**, 198001 (2017).
[11] G. I. Taylor, "Conical free surfaces and fluid interfaces," in *Applied Mechanics* (Springer, 1966), pp. 790–796.
[12] J. D. Buckmaster, "Pointed bubbles in slow viscous flow," J. Fluid Mech. **55**, 385–400 (1972).
[13] E. J. Hinch and A. Acrivos, "Steady long slender droplets in two-dimensional straining motion," J. Fluid Mech. **91**, 401–414 (1979).
[14] J. D. Sherwood, "Spindle-shaped drops in a viscous extensional flow," Math. Proc. Cambridge Philos. Soc. **90**, 529–536 (1981).
[15] M. S. Longuet-Higgins, "Bubbles, breaking waves and hyperbolic jets at a free surface," J. Fluid Mech. **127**, 103–121 (1983).
[16] M. S. Longuet-Higgins, "An analytic model of sound production by raindrops," J. Fluid Mech. **214**, 395–410 (1990).
[17] B. W. Zeff, B. Kleber, J. Fineberg, and D. P. Lathrop, "Singularity dynamics in curvature collapse and jet eruption on a fluid surface," Nature **403**, 401–404 (2000).
[18] S. P. Das and E. J. Hopfinger, "Parametrically forced gravity waves in a circular cylinder and finite-time singularity," J. Fluid Mech. **599**, 205–228 (2008).
[19] D. K. Raja, S. P. Das, and E. J. Hopfinger, "On standing gravity wave-depression cavity collapse and jetting," J. Fluid Mech. **866**, 112–131 (2019).
[20] J. M. Boulton-Stone and J. R. Blake, "Gas bubbles bursting at a free surface," J. Fluid Mech. **254**, 437–466 (1993).
[21] E. Ghabache, A. Antkowiak, C. Josserand, and T. Séon, "On the physics of fizziness: How bubble bursting controls droplets ejection," Phys. Fluids **26**, 121701 (2014).
[22] A. M. Gañán-Calvo, "Revision of bubble bursting: Universal scaling laws of top jet drop size and speed," Phys. Rev. Lett. **119**, 204502 (2017).

[23]S. Krishnan, E. J. Hopfinger, and B. A. Puthenveettil, "On the scaling of jetting from bubble collapse at a liquid surface," J. Fluid Mech. **822**, 791–812 (2017).
[24]C.-Y. Lai, J. Eggers, and L. Deike, "Bubble bursting: Universal cavity and jet profiles," Phys. Rev. Lett. **121**, 144501 (2018).
[25]R. Bergmann, D. van der Meer, M. Stijnman, M. Sandtke, A. Prosperetti, and D. Lohse, "Giant bubble pinch-off," Phys. Rev. Lett. **96**, 154505 (2006).
[26]R. Bergmann, D. van der Meer, S. Gekle, A. van der Bos, and D. Lohse, "Controlled impact of a disk on a water surface: Cavity dynamics," J. Fluid Mech. **633**, 381–409 (2009).
[27]S. T. Thoroddsen, K. Takehara, H. D. Nguyen, and T. G. Etoh, "Singular jets during the collapse of drop-impact craters," J. Fluid Mech. **848**, R3 (2018).
[28]J. Lu and C. M. Corvalan, "Dynamical transitions during the collapse of inertial holes," Sci. Rep. **9**, 14649 (2019).
[29]J. M. Gordillo and J. Rodríguez-Rodríguez, "Capillary waves control the ejection of bubble bursting jets," J. Fluid Mech. **867**, 556–571 (2019).
[30]J. Eggers and M. A. Fontelos, *Singularities: Formation, Structure, and Propagation* (Cambridge University Press, 2015).
[31]J. Eggers, M. A. Fontelos, D. Leppinen, and J. H. Snoeijer, "Theory of the collapsing axisymmetric cavity," Phys. Rev. Lett. **98**, 094502 (2007).
[32]S. T. Thoroddsen, T. G. Etoh, and K. Takehara, "Experiments on bubble pinch-off," Phys. Fluids **19**, 042101 (2007).
[33]R. Bolaños-Jiménez, A. Sevilla, and C. Martínez-Bazán, "The necking time of gas bubbles in liquids of arbitrary viscosity," Phys. Fluids **28**, 042105 (2016).
[34]J. C. Burton, R. Waldrep, and P. Taborek, "Scaling and instabilities in bubble pinch-off," Phys. Rev. Lett. **94**, 184502 (2005).
[35]X. F. Jiang, C. Zhu, and H. Z. Li, "Bubble pinch-off in Newtonian and non-Newtonian fluids," Chem. Eng. Sci. **170**, 98–104 (2017).
[36]J. C. Burton and P. Taborek, "Role of dimensionality and axisymmetry in fluid pinch-off and coalescence," Phys. Rev. Lett. **98**, 224502 (2007).
[37]X. Xia, C. He, and P. Zhang, "Universality in the viscous-to-inertial coalescence of liquid droplets," Proc. Natl. Acad. Sci. U. S. A. **116**, 23467–23472 (2019).
[38]J. M. Gordillo and M. Pérez-saborid, "Axisymmetric breakup of bubbles at high Reynolds numbers," J. Fluid Mech. **562**, 303–312 (2006).
[39]J. M. Gordillo, A. Sevilla, J. Rodríguez-Rodríguez, and C. Martinez-Bazan, "Axisymmetric bubble pinch-off at high Reynolds numbers," Phys. Rev. Lett. **95**, 194501 (2005).
[40]M. A. Fontelos, J. H. Snoeijer, and J. Eggers, "The spatial structure of bubble pinch-off," SIAM J. Appl. Math. **71**, 1696–1716 (2011).
[41]J. Miles and D. Henderson, "Parametrically forced surface waves," Annu. Rev. Fluid Mech. **22**, 143–165 (1990).